High-Frame-Rate Contrast-Enhanced Echocardiography Using Diverging Waves: 2-D Motion Estimation and Compensation

Luzhen Nie , *Student Member, IEEE*, David M. J. Cowell , Thomas M. Carpenter , James R. McLaughlan , Arzu A. Çubukçu, and Steven Freear , *Senior Member, IEEE*

Abstract—Combining diverging ultrasound waves and microbubbles could improve contrast-enhanced echocardiography (CEE), by providing enhanced temporal resolution for cardiac function assessment over a large imaging field of view. However, current image formation techniques using coherent summation of echoes from multiple steered diverging waves (DWs) are susceptible to tissue and microbubble motion artifacts, resulting in poor image quality. In this study, we used correlation-based 2-D motion estimation to perform motion compensation for CEE using DWs. The accuracy of this motion estimation method was evaluated with Field II simulations. The root-mean-square velocity errors were 5.9% ± 0.2% and 19.5% ± 0.4% in the axial and lateral directions, when normalized to the maximum value of 62.8 cm/s which is comparable to the highest speed of blood flow in the left ventricle (LV). The effects of this method on image contrast ratio (CR) and contrast-to-noise ratio (CNR) were tested *in vitro* using a tissue mimicking rotating disk with a diameter of 10 cm. Compared against the control without motion compensation, a mean increase of 12 dB in CR and 7 dB in CNR were demonstrated when using this motion compensation method. The motion correction algorithm was tested *in vivo* on a CEE data set acquired with the Ultrasound Array Research Platform II performing coherent DW imaging. Improvement of the B-mode and contrast-mode image quality with cardiac motion and blood flow-induced microbubble motion was achieved. The results of motion estimation were further processed to interpret blood flow in the LV. This allowed for a triplex cardiac imaging technique, consisting of B mode, contrast mode, and 2-D vector flow imaging with a high frame rate of 250 Hz.

Index Terms—Diagnostic ultrasound, diverging wave (DW) imaging, echocardiography, high-frame-rate (HFR) ultrasound, microbubbles, motion compensation, motion estimation, myocardial perfusion, ultrasound contrast agents, vector flow imaging.

L. Nie, D. M. J. Cowell, T. M. Carpenter, and S. Freear are with the Ultrasonics and Instrumentation Group, School of Electronic and Electrical Engineering, University of Leeds, Leeds, LS2 9JT, U.K. (e-mail: elln@leeds.ac.uk; s.freear@leeds.ac.uk).

J. R. McLaughlan is with the Ultrasonics and Instrumentation Group, School of Electronic and Electrical Engineering, University of Leeds, Leeds, LS2 9JT, U.K., and also with the Leeds Institute of Cancer and Pathology, University of Leeds, Leeds, LS9 7TF, U.K.

A. A. Çubukçu is with the East Cheshire NHS Trust, Macclesfield, SK10 3BL, U.K.

I. INTRODUCTION

MICROBUBBLES are micron-sized spheres with a heavy gas core that is stabilized by a shell made of lipids, polymers, proteins, or surfactants [1]. Due to their significant acoustic impedance mismatch relative to the surrounding tissue and blood cells, they are excellent ultrasound scatters and have long been used as ultrasound contrast agents [2]. Additional advances in understanding their nonlinear oscillations, when subject to an ultrasound field, underpin a number of microbubble-specific detection techniques such as pulse inversion (PI) [3] and amplitude modulation (AM) [4], granting insight into the microcirculation and hence perfusion [5], [6].

In cardiology, the use of microbubbles is recommended when more than 20% of the left ventricle (LV) endocardium is not clearly visible [7]. Contrast-enhanced echocardiography (CEE) is routinely used in the clinic for LV opacification, endocardial border definition, regional wall motion assessment, and LV mass diagnosis, among others [8], [9]. However, most conventional echocardiography is limited by a tradeoff between the imaging field of view, temporal resolution, and spatial resolution due to the use of the conventional line-by-line scanning [10]. For 2-D ultrasound imaging, a typical frame rate ranging from 30 to 80 Hz [11] is sufficient for assessment of cardiac morphology but insufficient for resolving short-lived cardiac events such as isovolumic acceleration [10] or complex intracardiac blood flow [12]. The accurate estimation of ventricular flow patterns by CEE using regular frame rates together with Navier–Stokes regularization has been demonstrated [13] but a substantial cutoff for the estimation of the high velocities exists due to the limited frame rate. Thus, the use of high-frame-rate (HFR) CEE with a large imaging field of view could lead to better assessment of cardiac function through visualization and quantification of transient events not captured with current CEE techniques.

Improving the temporal resolution of echocardiography is an active area of research [10]. One method is multiline acquisition (MLA) [14], wherein multiple receiving lines, typically 4 [10], are beamformed simultaneously from one weakly-focused transmission. However, the broadened beam in this method results in reduction of lateral resolution. Recent engineering advances in open ultrasound platforms such as the customization of the transmit waveform on each channel [15], have allowed for the development of new

HFR cardiac imaging techniques. Multiline transmission is an example of this, and considered an alternative approach to MLA [16]–[18]. In this technique, multiple focused ultrasound beams, typically 4 [11], are simultaneously transmitted to reduce the time needed to sweep the whole region of interest (ROI). However, these multiple transmit beams overlap in the nearfield [19], which might disrupt microbubbles significantly due to the increased mechanical index, limiting its use for contrast-enhanced ultrasound. Another alternative to MLA is to transmit nonfocused diverging waves (DWs) [20]–[25], where a full field-of-view 2-D image can be reconstructed from a single transmission. The image degradation due to the lack of transmit focusing can be minimized by coherent spatial compounding [21] by sacrificing the imaging frame rate. As with synthetic transmit aperture imaging [26]–[29] and coherent plane wave imaging [30], [31], where synthetic summation of low-resolution images (LRIs) is required for a high-resolution image (HRI), coherent DW imaging is susceptible to motion artifacts. The complex and nonrigid motion of the myocardium [17] and pulsatile microbubble populations [32] in the heart chambers could result in these artifacts, causing contrast and spatial resolution degradations in the compound image. Thus, further development of methods to preserve the efficacy of spatial compounding for HFR CEE using DWs is needed.

Doppler-based motion compensation has been proposed for HFR echocardiography using DWs [11], [33]. This technique which only accounts for axial motion, works well for the compensation of myocardial motion but might not be ideal for HFR CEE. In the first instance, Doppler aliasing could happen in the LV, causing incorrect estimation and hence incorrect compensation. In addition, axial motion compensation alone could be insufficient when the total lateral motion is large in comparison to the wavelength [34], which might be true for the fast-flowing microbubbles in the LV. Recently, an image registration algorithm adapted from magnetic resonance imaging, was applied to HFR CEE using phase-inverted DWs [35], to correct motion artifacts *in vivo*. In this case, the determination of the reference frame is crucial and may result in compensation failure if the chosen reference frame has a low signal-to-noise ratio (SNR).

In this study, a two-stage motion estimation method was applied to HFR CEE using DWs [11], [12], to restore the quality of the coherent compound image by compensating for motion between steered DWs. This approach was evaluated both *in vitro* and *in vivo*. Without additional pulse transmissions, the results of motion estimation were also leveraged for 2-D vector blood flow mapping in the LV *in vivo*. This allowed for the implementation of a HFR triplex cardiac imaging tool, by simultaneously performing B-mode imaging, contrast-mode imaging, and 2-D vector flow mapping. Abbreviations in this manuscript are summarized in Table I.

II. MATERIALS AND METHODS

A. Motion Estimation and Compensation

In this study, the motion is defined as the combination of myocardial tissue motion, probe motion due to freehand

TABLE I
ABBREVIATIONS

Short name	Full name
PI	Pulse inversion
AM	Amplitude modulation
LV	Left ventricle
CEE	Contrast-enhanced echocardiography
HFR	High-frame-rate
MLA	Multiline acquisition
ROI	Region of interest
DW	Diverging wave
LRI	Low-resolution image
HRI	High-resolution image
SNR	Signal-to-noise ratio
RF	Radio frequency
UARP II	Ultrasound Array Research Platform II
PRF	Pulse repetition frequency
CR	Contrast ratio
CNR	Contrast-to-noise ratio
RMS	Root-mean-square

scanning, and blood flow-induced microbubble motion in heart chambers. We use a correlation-based 2-D motion estimation method to get subpixel displacements between adjacent tilted DW emissions. Based on these estimated displacements, motion compensation is then performed by aligning image pixels of all LRIs prior to coherent summation. For motion compensation in ultrasound imaging using unfocused beams, the first LRI in the set [27], the central LRI [35], or the $(N/2)$th LRI (where N is even) [11] has been used as the reference for registration. In this study, all LRIs are heuristically registered to the first LRI within the sequence that is used for coherent compounding. The processing chain is shown in Fig. 1.

1) Two-Stage Motion Estimation: A constant velocity for each estimation point was assumed during transmitting a DW compounding sequence (a 4 ms period in this paper as given in Section II-B). Two-stage motion estimation was applied to the beamformed radio frequency (RF) LRIs prior to coherent compounding in the polar grid. The first stage used rigid block matching [36] with interrogation windows of identical size, and the second used iterative window refinement to improve resolution. Both stages were based on cross correlation.

To improve the robustness of the coarse estimations in the first stage, block matching was performed with correlation correction [37], achieved by sequentially multiplying all available correlation maps from successive pairs of LRIs. Cross correlation was performed in the frequency domain and the peaks in the correlation functions were used to estimate the average displacements of interrogation windows. The subpixel motion estimations were then found by fitting the three-point Gaussian function in the proximity of the correlation peak [38].

In the second stage, an iterative scheme was adopted for each pair of adjacent LRIs, wherein the interrogation windows were resized and deformed based on the results of motion estimation from a previous iteration. Window resizing was performed with the current window having a half radial
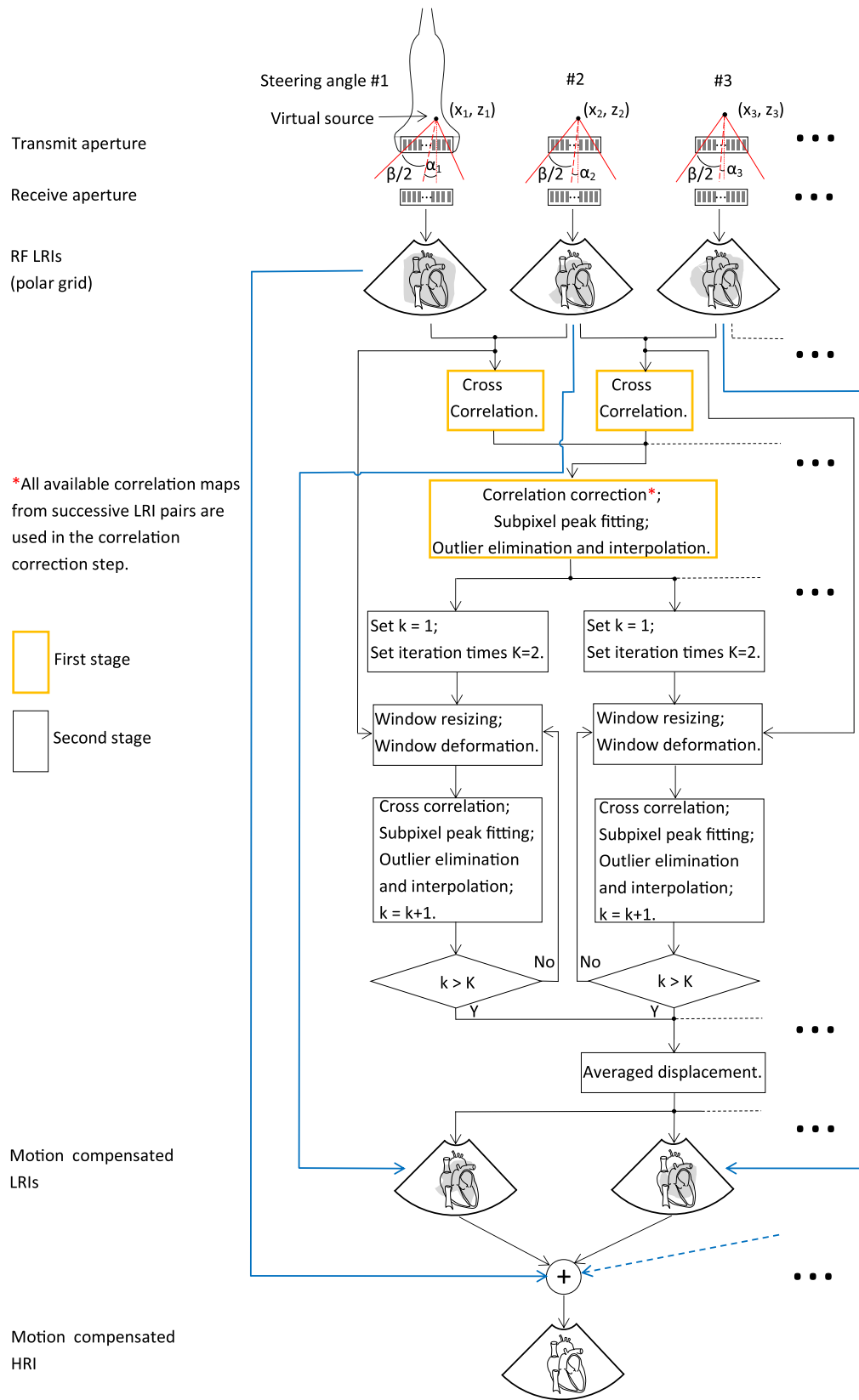
Fig. 1. Workflow of the proposed DW imaging approach with motion compensation. Motion estimation and compensation are performed within a pulse sequence that is used to form a HRI. β is not changed for different steering angles. α_1, α_2, and α_3: steering angles. β: angular width. RF: radio frequency.

size and a half angular size compared to the values used in the previous iteration. Window deformation was used for accommodating nonrigid motion and it was achieved by the first-order approximation of the local displacement field [38], [39]. The second stage was initialized with a motion estimation field from the first stage, as shown in Fig. 1. In each

iteration, new cross correlation functions were performed using the size-reduced and deformed interrogation windows and the remaining displacement was accumulated to improve the local estimation accuracy. As the interrogation window size was further decreased in each iteration, the spatial resolution of motion estimation was improved. But there was a tradeoff between the spatial resolution of motion estimation (a smaller window size) and the computational complexity because of the need of more iterations. The maximum number of iterations was fixed to two in this study and more discussion about this arrangement can be found in Section IV-A. Between the iterations, subpixel peak fitting was also performed on the new cross correlation functions which improved the accuracy of window deformation [38].

A local median filter [40]($\varepsilon = 0.02$, threshold = 2, $b = 1$) and a filtering method [33] using global standard deviations ($\delta = 5$) were used to remove outliers for the first stage and each iteration in the second stage. Outlier vectors were replaced with linear interpolated values from nearest neighbors and the results of motion estimation were then smoothed by means of a least-squares method [41]. After two iterations, the displacement information at the center of each interrogation window was found with each successive pair of LRIs. For each interrogation window, the displacement estimations from all successive pairs of LRIs were averaged to improve the accuracy. The displacement for each pixel was then obtained by linearly interpolating these averaged displacements at the window centers.

2) Application of Motion Compensation to HFR CEE Using DWs: A nonlinear imaging scheme AM [4] was used for HFR CEE in this study. At each steering angle, a two-pulse AM packet was transmitted, with the first pulse transmission having a full amplitude and the second one having a half amplitude. The echo from the full-amplitude transmission and twice of the sign-inverted echo from the half-amplitude transmission were combined before compounding. With the full-amplitude transmissions, a synchronized B-mode imaging sequence was acquired.

In comparison to half-amplitude transmissions, the full-amplitude transmissions provided an improved SNR. Two-stage motion estimation was thus performed on the LRIs from full-amplitude transmissions. Relocation of the image pixels was then applied to both low-resolution B-mode (RF) images and AM contrast-mode (RF) images before coherently summing them together. Linear interpolation of the LRI intensities was adopted to accommodate the subpixel accuracy of the motion estimations.

B. Imaging Setup

For DW imaging, four-cycle 2.78 MHz ultrasound pulses with either a full or half amplitude were transmitted, emulating DWs using the full aperture [11]. The four-cycle excitation signals were tapered using a Tukey window with a coefficient of 0.2. The angular width β that was determinant to the imaging field of view was set to 90°, as used in [11]. All *in vitro* and *in vivo* measurements were performed with the University of Leeds Ultrasound Array Research Platform II (UARP II) equipped with a Verasonics P4-2v transducer

TABLE II
PARAMETERS FOR BOTH *in vitro* AND *in vivo* MEASUREMENTS

Parameter	Value
Apodization in transmit	Rectangular window
Apodization in receive	Rectangular window
Sampling frequency for transmit	160 MHz
Sampling frequency for receive	20 MHz
Angular width β	90°
PRF	4 kHz
Imaging scheme	AM (see Section II-A2)
Steering angles	(−10°, −8°, −6°, −4°,
	4°, 6°, 8°, 10°)
Excitation signal	4-cycle sinusoid (2.78 MHz)
Tapering function on excitations	Tukey (coefficient: 0.2)
Mechanical index	0.12 (derating factor:
	0.3 dB/MHz/cm)

(Verasonics, Inc., WA, USA). The UARP II is capable of arbitrary waveform generation on each channel [42], [43] which permits the accurate pressure modulation needed for nonlinear contrast-enhanced imaging with AM. The phased array transducer P4-2v had a −6 dB bandwidth of 60% and a center frequency of 2.78 MHz. Acoustic pressures were measured at room temperature (21 °C) in degassed and deionized water with a calibrated 200 μm needle hydrophone (Precision Acoustics, Dorchester, UK). The *in situ* mechanical index [44], [45] was set to 0.12 with a derating factor of 0.3 dB/MHz/cm. The parameters for both *in vitro* and *in vivo* measurements are given in Table II. For both B-mode and contrast mode imaging in this study, a Hamming window was used to design a bandpass filter with cutoff frequencies at 1.9 MHz and 3.6 MHz, matching the −6 dB bandwidth of the transducer.

To match the frame rate of 250 Hz as demonstrated in [11], [12], a sequence of 16 pulse transmissions (two-pulse AM packet at each steering angle as illustrated in Section II-A2) was designed with a PRF of 4 kHz. To facilitate coherent compounding, the DWs were steered at varied angles while keeping the angular width β unchanged. The step between steering angles for motion estimation was fixed to 2° which is similar to 1.8° in [33]. Instead of using a pulse sequence with a constant angle step (−7°: 2°: 7°), the maximum steering angle was heuristically set to 10°. The resulting arrangement for steering angles was: −10°, −8°, −6°, −4°, 4°, 6°, 8°, and 10°. This approach was to achieve an improved lateral resolution with coherent compounding, as the larger angular range gives lower sidelobe levels for the equivalent number of steering angles [46]. The improved lateral resolution with the proposed sequence was demonstrated by measuring a point spread function using the UARP II. In degassed and deionized water, a wire target with a diameter of 150 μm was placed at the depth of 60 mm relative to the transducer surface, which matched the elevation focus of the transducer. The improved −6 dB lateral resolution of 2.1 mm was obtained when using the proposed sequence for both fundamental B-mode imaging and the contrast mode using AM. While this value was 2.3 mm with the normal sequence that used an equal angle step (−7°: 2°: 7°). However, regardless

Parameter	Value
Number of elements	64
Pitch size	0.3 mm
Element height	13 mm
Elevation focus	60 mm
Center frequency	2.78 MHz
Bandwidth (-6 dB)	60%
Speed of sound	1540 m/s
Sampling frequency for transmit	160 MHz
Sampling frequency for receive	20 MHz
Excitation signal	4-cycle sinusoid (2.78 MHz)
Tapering function on excitations	Tukey (coefficient: 0.2)
Apodization in transmit	Rectangular window
Apodization in receive	Rectangular window
Angular width β	90°
Steering angles	($-10°$, $-8°$, $-6°$, $-4°$, 4°, 6°, 8°, 10°)

TABLE IV
PARAMETERS FOR BEAMFORMING AND MOTION ESTIMATION

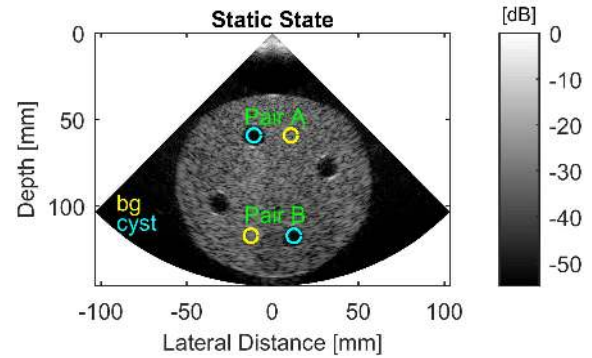| Parameter	Value
Radial pixel size	38.5 μm
Angular pixel size	0.0625°
Window size (1st stage)	152x84 (radial and angular lines)
Window size (2nd stage)	76x42; 38x21
Window overlap	50%

Fig. 2. Illustration of ROIs used for quantitative analysis of CR and CNR. All circular ROIs have a diameter of 8 mm. bg: background.
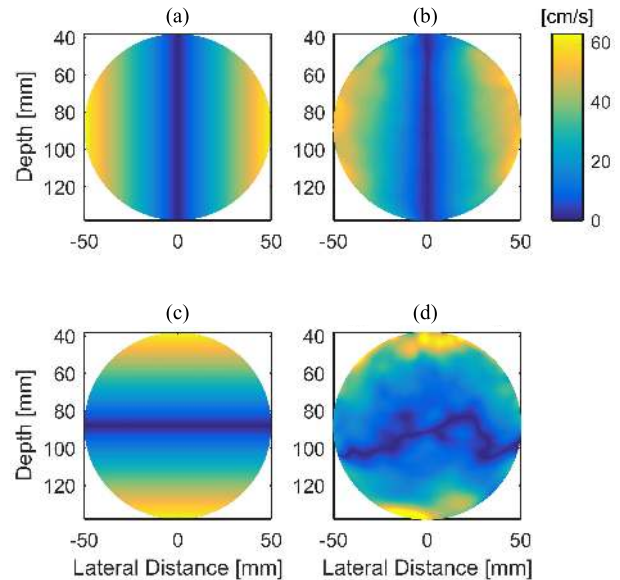

Fig. 3. Estimated absolute velocities in the axial and lateral directions using Field II are compared to their theoretical true values. The values are reported from one simulation. (a) True V_z. (b) Estimated V_z. (c) True V_x. (d) Estimated V_x. V_z: velocity in the axial direction and V_x: velocity in the lateral direction.

of the optimization, motion will always interfere with coherent DW compounding. This paper focuses on the demonstration of the feasibility to make motion compensation to preserve the quality of HFR CEE when using DWs.

C. Evaluation With a Rotating Disk

1) Accuracy of Motion Estimation: The accuracy of the motion estimation method was evaluated by using Field II simulations [47]. The transducer P4-2v that was used for both *in vitro* and *in vivo* measurements was simulated. Acoustic attenuation was not considered in the calculation. As motion estimation was performed with the linear LRIs from full-amplitude ultrasound pulses, AM pulse transmissions were not simulated. The simulation parameters are given in Table III. A cylindrical phantom was simulated with a density of 10 scatters per resolution cell, generating a fully developed speckle pattern [28]. It had a thickness of 10 mm in the elevation direction and a disk diameter of 10 cm. No anechoic cysts were embedded. The phantom was placed at the depth of 88 mm and rotated at 4π rad/s with repeated insonifications by the 8 pulse transmission sequence ($-10°$, $-8°$, $-6°$, $-4°$, 4°, 6°, 8°, and 10°) at a PRF of 2 kHz. The velocity of the disk achieved its maximum at the outer boundary with a value of 62.8 cm/s which is comparable to the highest speed of blood flow in the LV [48]. In all simulations, white Gaussian noise was added to the RF data before beamforming giving an SNR of 30 dB.

The raw data sets were beamformed in a polar grid (90° wide) using the delay-and-sum approach in MATLAB (The MathWorks, Natick, MA, USA). Two-stage motion estimation was then performed with LRIs. The parameters used for beamforming and motion estimation are summarized in Table IV. The estimated subpixel-wise displacements were then used to counter-shift the LRIs and correct for incoherence between angled DWs, enabling coherent compounding. Operation details of motion estimation and compensation are given in Section II-A. Motion estimation between the frames with steering angles $-4°$ and $4°$ was not performed because of the large angular step of 8° (2° between other steered DWs) and the associated low image correlation [49]. More discussion about this operation is given in Section IV-A.

The root-mean-square (RMS) velocity errors [24] were calculated from ten repeat simulations, with a different noise value added to each repeat. The RMS velocity errors were then normalized to the maximum speed of the disk.
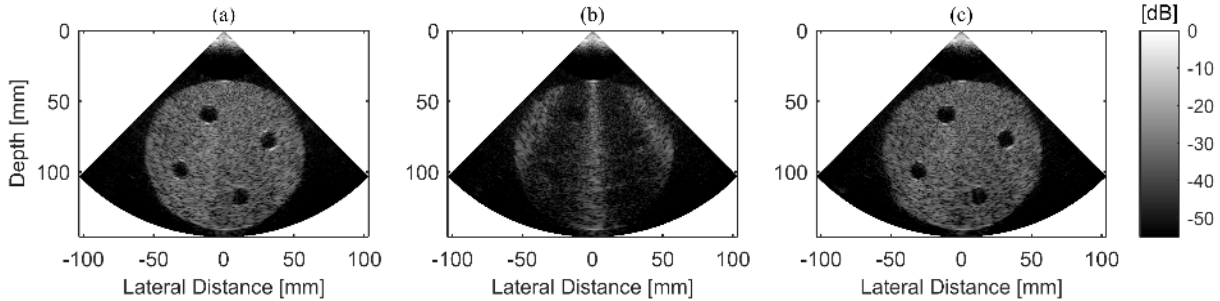
Fig. 4. Compound images of the *in vitro* disk in the (a) static state and rotating state (b) without and (c) with motion compensation. The *in vitro* disk was rotated at 4π rad/s in (b) and (c).

2) Effects of Motion Compensation on Image Quality: An agar-based tissue-mimicking rotating disk [50] was fabricated for evaluating the effect of the proposed method on image quality *in vitro*. The average speed of sound and attenuation through this phantom was 1540 m/s and 0.55 dB/MHz/cm, respectively [51]. The disk had a 10 cm diameter and four equidistant 12.8-mm anechoic cysts located at 32 mm relative to the disk center. It was mounted to the shaft of a stepper motor controlling the rotation speed at 4π rad/s. The phantom was placed at the same depth of 88 mm as used for simulations. The ultrasound parameters are given in Table II. The effect of motion compensation was investigated only on B-mode imaging due to the absence of microbubbles. The benchmark of these measurements was determined by imaging the disk in a static state. Beamforming, motion estimation and compensation were performed off line using MATLAB (Table IV).

The performance of the proposed method was quantitatively analyzed by calculating the contrast ratio (CR) and contrast-to-noise ratio (CNR) with the ROIs as shown in Fig. 2 [52]

$$\text{CR} = 20\log_{10}\left(\frac{\mu_{\text{bg}}}{\mu_{\text{cyst}}}\right) \tag{1}$$

$$\text{CNR} = 20\log_{10}\left(\frac{\mu_{\text{bg}} - \mu_{\text{cyst}}}{\sqrt{\sigma_{\text{bg}}^2 + \sigma_{\text{cyst}}^2}}\right) \tag{2}$$

where μ_{bg} and μ_{cyst} are the mean image intensities (enveloped data before log compression) within the background and cyst regions. σ_{bg} and σ_{cyst} denote their corresponding standard deviations.

Two pairs of 8-mm diameter ROIs at different depths were defined in Fig. 2 and two ROIs in each pair were positioned at the same depth.

D. In Vivo Investigations

The *in vivo* data of apical two-chamber view was acquired from a healthy volunteer using the UARP II. The acquisition was performed with handheld scanning utilizing the same probe and acoustic parameters used for *in vitro* validation (Table II). A 1 mL bolus of SonoVue microbubbles (Bracco S.p.A, Milan, Italy) was administrated followed by a 4 mL saline flush. The on-line B-mode imaging sequence using focused beams was used to guide the probe alignment and time the trigger of the AM DW sequence after the arrival of microbubbles in the LV. For real-time imaging feedback, the beams were focused at the depth of 10 cm with an *in situ* mechanical index of 0.25. The corresponding excitation signal was a three-cycle 2.5 MHz sinusoid tapered with a Tukey window (coefficient: 0.5). The AM DW scanning lasted for 1.4 s covering one cardiac cycle and the corresponding data was subsequently postprocessed in MATLAB.

The operation of beamforming and motion estimation was carried out with the parameters shown in Table IV, except the imaging depth was decreased to 12.6 cm from 14.6 cm to cover the LV. The RF images from the full-amplitude transmissions were used for motion estimation and compensation was then applied to both B-mode imaging and contrast-mode imaging. The results of motion estimation were simultaneously leveraged for 2-D vector blood flow mapping in the LV. No temporal averaging was applied to smooth the velocity profile.

III. RESULTS

A. Rotating Disk Studies

1) Accuracy of Two-Stage Motion Estimation: Fig. 3 shows the absolute velocities from the Field II simulation. These results show that the axial motion estimation was more accurate than the lateral motion estimation. Based on ten repeat simulations, the RMS velocity errors were 5.9% $\pm$ 0.2% and 19.5% $\pm$ 0.4% for the axial and lateral directions, respectively. In addition to improving the quality of the compound images, the results of motion estimation could be encoded to depict the complex blood flow patterns in the LV as demonstrated later in Section III-B.

2) Effects of Motion Correction on Image Quality: The images in Fig. 4, from left to right, show the *in vitro* disk in the static state as benchmark, in the spinning state without and with the integration of motion compensation, respectively. In comparison to Fig. 4(a), the benchmark, direct coherent DW imaging in the presence of motion resulted in substantial artifacts due to incoherence between angled DWs, as shown in Fig. 4(b). Qualitatively, exploiting motion between angled DWs and applying motion compensation to LRIs prior to compounding yielded a significant improvement in image quality as shown in Fig. 4(c).

Quantitatively, the CRs and CNRs for two pairs of ROIs as given in Fig. 2 are summarized in Fig. 5. Both CRs and CTRs have been restored for ROI pairs A and B with motion compensation, obtaining comparable values to the references in all cases. Without motion compensation, the CR and CTR
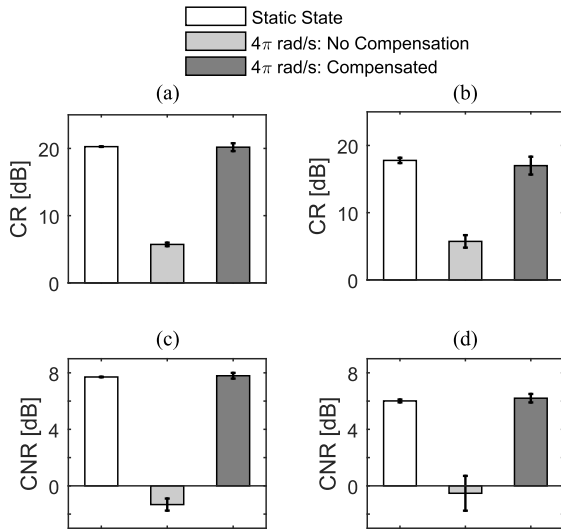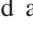
Fig. 5. Quantitative CRs and CNRs for two pairs of ROIs as shown in Fig. 2. The mean values and standard deviations are from four repeat measurements. (a) CR: ROI Pair A. (b) CR: ROI Pair B. (c) CNR: ROI Pair A. (d) CNR: ROI Pair B.

have decreased by approximately 12 dB and 7 dB (mean values for two ROI pairs). The depth of the ROI affected the standard deviations for both CRs and CNRs. A larger standard deviation was observable for all measurements in ROI pair B, placed at a deeper location. Due to acoustic attenuation, a lower SNR is expected in a deeper region, accounting for this observation. But without the application of motion compensation, the information in the compound image [Fig. 4(b)] has been lost.

B. In Vivo Results

Fig. 6 shows beamformed frames from the DW scanning sequence covering one cardiac cycle. Two full video clips are provided as the supplementary material (Supplementary Video S1▣, played back at its acquisition rate of 250 frames per second and Supplementary Video S2▣, played back at 50 frames per second).

The quality of the *in vivo* cardiac images was improved when integrated with motion compensation (Fig. 6). This improvement was visible on B-mode images. For example, without the use of motion compensation, the microbubbles appeared to be unevenly distributed in the LV, resulting in a total dark region in the vicinity of the septum [Fig. 6(a)]. However, when using compensation it is clear that the microbubbles were present throughout the LV [Fig. 6(b)]. This enhancement can also be applied to contrast-enhanced imaging, which benefits from the preserved efficiency of coherent compounding with motion correction when comparing Fig. 6(c) and (d). The contrast-to-tissue ratio (CTR) [53] between the LV [green box in Fig. 6(b)] and the surrounding tissue region [red box in Fig. 6(b)] was calculated for Fig. 6(c) and (d). The delineation of the endocardial border is enhanced thanks to the improvement of CTR in Fig. 6(d) [10.8 dB compared to 1.3 dB in Fig. 6(c)]. The results of motion estimation for Fig. 6(b) and (d) were further processed to render blood flow vectors in the LV. The combination of vector flow mapping and

B-mode imaging is shown in Fig. 7. These flow vectors were from the last-iteration motion estimation but with a decimation factor of 1/4 along both directions for clarity. Two full videos showing 2-D vector blood flow mapping in the LV have been integrated within the same supplementary material including B-mode and contrast-mode images. Fig. 7 demonstrates that the blood flow reaches its maximum velocity within the same region that is dark in Fig. 6(a) and (c).

IV. DISCUSSION

Motion is unavoidable in ultrasound imaging, with induced artifacts present as geometric distortion of organ structures when using the focused-beam imaging paradigm but present as significant deterioration of image contrast/resolution when using coherent DW imaging. For HFR CEE using DWs, correction of probe, myocardial and microbubble motion in the LV is necessary to restore the image quality impaired by incoherence between the angled DWs. Compensation of blood flow-induced microbubble motion in the LV proved beneficial to segment myocardium with an improved CTR, as shown in Fig. 6(d). This demonstrates the relevance of the proposed motion compensation method for this application *in vivo*. A synchronized B-mode imaging sequence is also available in other nonlinear imaging schemes including PI and contrast pulse sequences (CPS). This approach could be used to correct motion artifacts for coherent DW imaging based on PI and CPS.

A. Selection of Parameters

As values reported in Fig. 5 are parameter related, they could change as a function of multiple parameters including the arrangement of steering angles, beamforming setup, sampling frequency, and motion estimation setup, among others. The number of DWs used for one compound image could be changed as long as the assumption of a constant velocity during the acquisition can be satisfied. In this study, the velocity was assumed to be constant within a 4 ms period (16 pulse transmissions with a PRF of 4 kHz) and the improved image quality with motion compensation was demonstrated *in vivo*. The motion estimation scheme proposed in this paper has two stages, with the first stage giving the global starting point as the input of the second stage that comprises iterative window refinement. Fig. 8 shows the effect of the number of iterations in the second-stage motion estimation on the RMS velocity errors. The same parameters in Section II-C1 were used except that the number of iterations was varied. In this study, the number of iterations for the second-stage motion estimation was set to two, from which the curve in Fig. 8 starts to flatten.

A tilt angle step of 2° which is similar to 1.8° in [33] was chosen for motion estimation in this study. However, the determination of this step is a compromise between the accuracy of motion estimation and the lateral resolution of the compound image. For example, a small tilt angle step enables a high correlation between DWs, benefiting accurate motion estimation. A large tilt angle step provides a better lateral resolution after compounding due to a low correlation
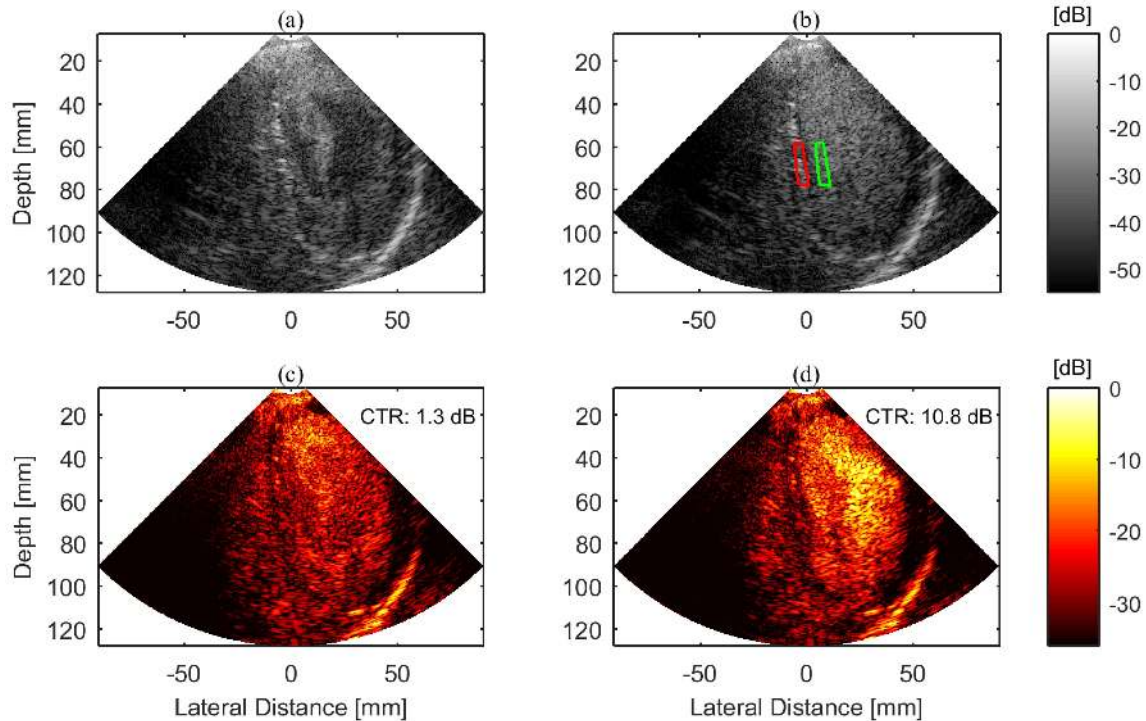
Fig. 6. Synchronized B-mode and contrast-mode compound images from the same AM pulse sequence consisting of 16 pulse transmissions. (a) B-mode: No compensation. (b) B-mode: Compensated. (c) Contrast-mode: No compensation. (d) Contrast-mode: Compensated. All 16 transmissions were used for (c) and (d), and 8 full-amplitude transmissions were combined for (a) and (b).
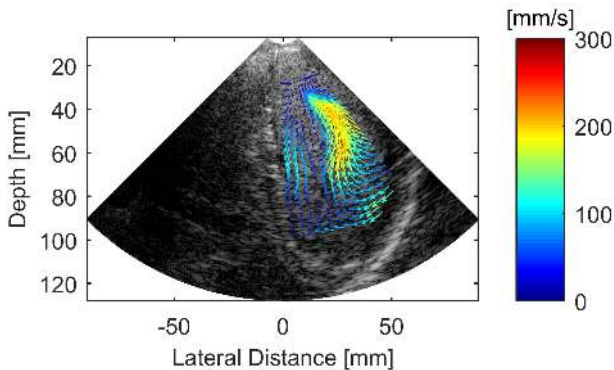

Fig. 7. Composite image of the LV by superimposing flow vectors onto its corresponding B-mode image. These two types of information were obtained from the same RF data as used for Fig. 6. The B-mode background is the same as shown in Fig. 6(b).
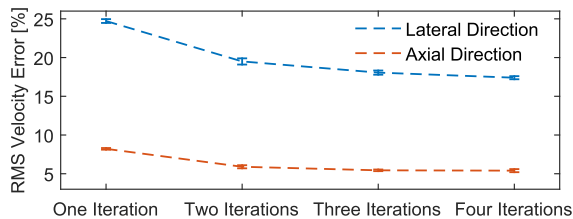

Fig. 8. Relationship between the RMS velocity error and the number of iterations in the second-stage motion estimation. Results are from ten repeat simulations.

between DWs [49]. For the adopted imaging sequence in this study, the suitability of excluding the LRI pair with steering angles of −4° and 4° for motion estimation was demonstrated by using the Field II simulated rotating disk. The relationship

between the angular step θ (2° or 8°) and the accuracy of motion estimation was investigated using a single pair of LRIs from the steering angles of −θ/2 and θ/2. All other parameters were identical to those in Section II-C1. For the angular step of 2°, the axial and lateral RMS velocity errors were 7.4% ± 0.1% and 23.2% ± 0.4%, respectively. While for the angular step of 8°, the corresponding errors increased to 9.9% ± 0.3% and 27.9% ± 0.6%, respectively. All values here are based on ten repeat simulations.

The most accurate velocity estimation occurs along the direction of beam propagation [54]. For sector scanning using focused beams, the use of the beamformed images in the polar coordinate system other than the scan-converted images in the Cartesian coordinate system is more effective for the cross-correlation based motion estimation [55]. When using the Cartesian coordinate system, the estimation outliers mainly existed at locations with a large beam steering angle, where motion tracking didn't follow the propagation direction of the incident ultrasonic beam [55]. Here, the polar coordinate system was thus adopted for motion estimation and compensation. Furthermore, the initial window size for motion estimation in the first stage should be big enough to accommodate the maximum flow velocity for specific cases, while keeping a good motion estimation resolution by minimizing the window size [56]. The window size in this paper was heuristically determined according to the "one quarter rule" [57], where the interframe displacement should be smaller than one quarter of the window size along both directions. With the combination of the maximum number of iterations in the second stage, the achievable local precision of motion compensation would be determined. The use of more iterations could improve the
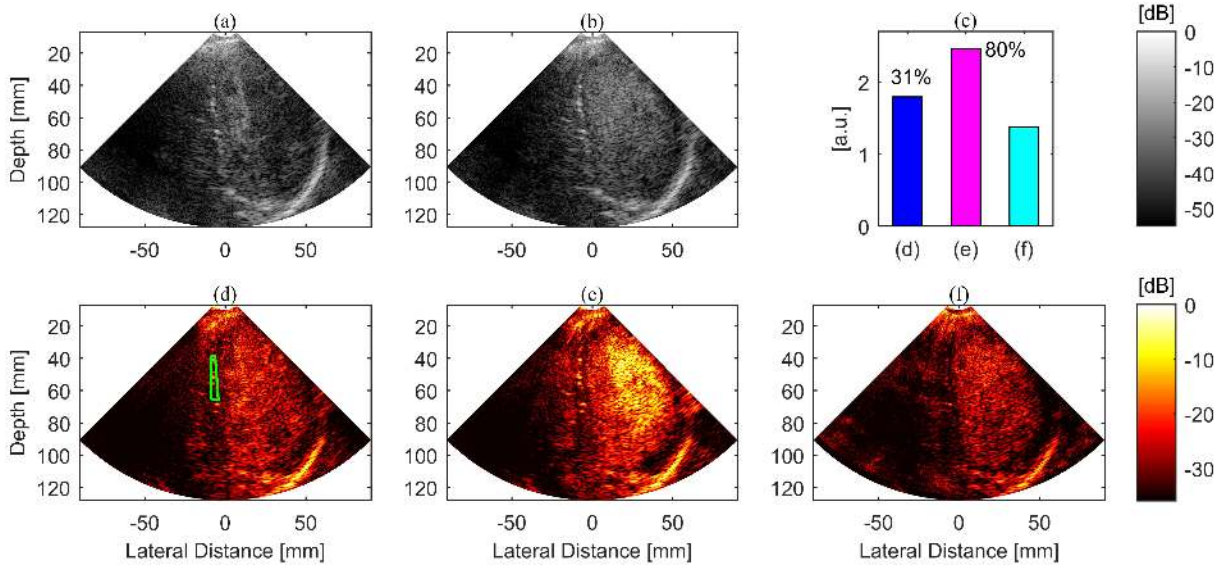
Fig. 9. B-mode compound images (a) before and (b) after motion compensation. Three contrast-mode images are shown in (d)–(f). (d) Without any motion compensation. (e) Only the motion artifacts between the AM LRIs were corrected. (f) When the motion artifacts within the AM pulse packet at each steering angle were also removed, apart from the motion compensation between the AM LRIs. For (d)–(f), intensity values for the myocardium ROI [marked in green on (d)] are shown in (c), where the percentage values marked show the differences in intensity of (d) and (e) relative to (f).

local accuracy for motion estimation and compensation but with higher computational cost.

B. Motion Artifacts Within the AM Pulse Packet

At each steering angle, motion compensation was not applied between the subsequent LRIs from the full and half-amplitude transmissions in the AM scheme. This is because in multipulse contrast-enhancement schemes such as the adopted AM, higher velocities cause the artificial CTR enhancement because of incoherent subtraction, which could be beneficial for visual inspection [58]. However, for the quantitative use of microbubbles such as myocardial perfusion imaging, compensation of myocardial motion within the AM pulse packet at each steering angle could be necessary, especially when the myocardium has a high speed as shown in Fig. 9. The effect of motion compensation is manifest for the myocardium, where the septum is poorly apparent in Fig. 9(a) when compared with Fig. 9(b). For the ROI of the myocardium, which is shown highlighted in green on Fig. 9(d), the image intensity in this region for each of Fig. 9(d)–(f) is shown in Fig 9(c). The myocardial motion causes the decorrelation of tissue signals within the AM packet, leaving a residual signal but treated as the microbubble contrast signal. This is obvious in Fig. 9(e), where the myocardium becomes hyperechoic in the contrast-mode compound image when only motion artifacts between the AM LRIs were corrected. Fig. 9(f) shows the contrast-mode compound image when the motion within the AM packet at each steering angle was also compensated for. Also marked in Fig. 9(c), the intensity differences within the ROI are 31% and 80% for Fig. 9(d) and (e) when compared to the intensity in Fig. 9(f), where all motion artifacts were removed. The linear relationship is usually made between the contrast-mode image intensity and the microbubble concentration in quantitative

myocardial perfusion studies [59]. The results suggest the necessity of removing the motion artifacts within the AM pulse packet for this application. This could also apply to other multipulse imaging schemes such as PI, where motion can interfere with the signal intensity [58].

C. Comparison With Existing Techniques

1) Doppler-Based Techniques: Though various Doppler-based techniques [11], [33], [60] have been proposed to perform motion compensation for HFR echocardiography using DWs, it would be difficult to implement these methods for HFR CEE. Since microbubbles can be selectively detected using nonlinear imaging schemes such as AM and PI at the cost of additional pulse transmissions, reducing the effective PRF and thus lowering the maximum detectable velocity without Doppler aliasing. With the motion compensation method in [11], [33] and [60], the reliable Doppler estimation was reported to be as high as a half of the classical Nyquist Doppler velocity, i.e., $cPRF/(8f_0)$, where c indicates the speed of sound and f_0 is the center frequency of the ultrasound pulse. Considering 1540 m/s and 2.78 MHz for c and f_0 in this study, the reliable Doppler estimation for motion compensation can be made up to a threshold of 0.138 m/s with the halved PRF at 2 kHz by using AM. Doppler aliasing is likely in the LV, where blood flow can exceed this threshold as demonstrated in Fig. 7. In addition, the phase autocorrelation [61], [62] in color Doppler could be biased in the presence of microbubbles due to their nonlinear vibrations [63], leading to incorrect motion compensation. In [11] (Fig. 7), the Doppler-based motion compensation method with a linear tilt sequence caused a smeared background in a rotating disk experiment but this artifact was not observed in Fig. 4 in the current study. This could be explained by that our method uses 2-D
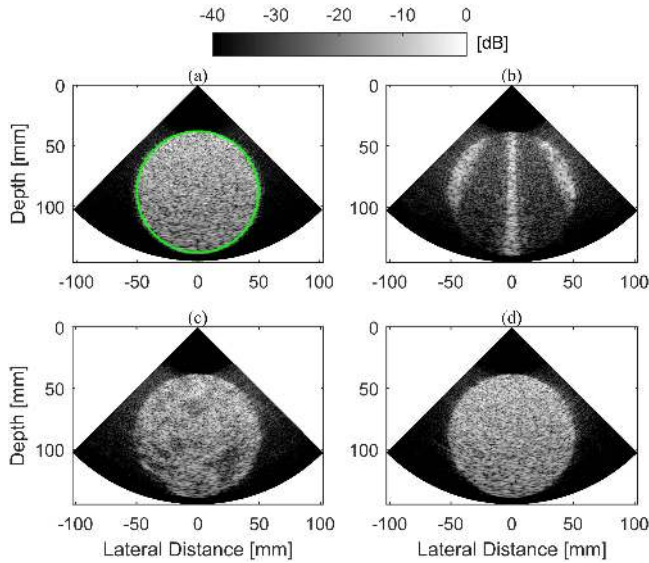
Fig. 10. Compound images of the Field II simulated disk in (a) the static state, the rotating state (b) without motion compensation, the rotating state compensated with (c) the image registration-based technique and (d) the proposed method. The simulated disk was rotated at 4π rad/s in (b)-(d). The circular ROI in (a) was used for calculating the image intensities. IR: image registration.

Fig. 11. Image intensities within the circular ROI as shown in Fig. 10(a) for Fig. 10(a)–(d). The values are the mean differences relative to the intensity without motion based on ten repeat simulations. IR: image registration.

pattern matching that is insensitive to the phase shift induced by sidelobes.

2) Image Registration Techniques: The central LRI with the steering angle of zero degree was used as the reference in [35], where an image registration model [64] was adopted for motion compensation in HFR CEE using DWs. For comparison studies, the rotating disk simulated with Field II and all imaging parameters adopted in Section II-C1 were used, except that the steering angles were changed to [$-8°$, $-6°$, $-4°$, $-2°$, $0°$, $2°$, $4°$, $6°$, and $8°$] to have the zero-degree transmission. The motion estimation and correction method in Section II-C1 was performed and all LRIs were registered to the central frame. Because of the equal angular step of $2°$ between all steering angles, all LRI pairs were used for motion estimation. For comparison, the image registration model [64] was also applied to the LRIs in the polar grid before coherent compounding. During image registration, the default parameters for 2-D images [65] were used. Fig. 10(a) and (b) show the disk without motion and in the state of rotation but without motion compensation. With motion correction using the image registration technique, coherent DW compounding was partially improved, with the disk boundary visible as shown in Fig. 10(c). While correction of the boundary is apparent, dark artifacts appear as smears in the corrected image which makes interpretation difficult. Conversely, with the proposed method, the artifacts from the original image were totally removed without any smearing of the image as shown in Fig. 10(d). The image intensities within the circular ROI as shown in Fig. 10(a) are given in Fig. 11. The method in this paper outperforms the image registration technique, with a smaller intensity bias and a smaller intensity variation relative to the values without motion (Fig. 11). The robustness of the restored image intensity could be particularly beneficial for the
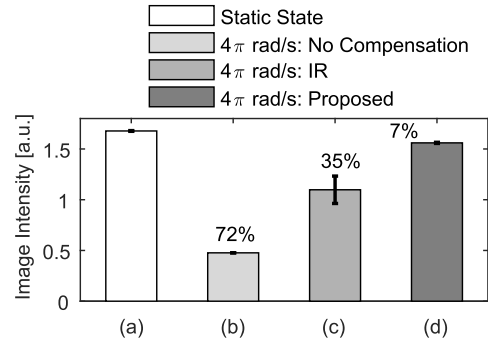
quantitative applications of microbubbles such as myocardial perfusion imaging.

D. Future Development

The method was performed by using MATLAB R2017a and executed on a CPU (Intel Xeon, E-5-1620, 3.6 GHz). The computation time of motion estimation and compensation for one compound image in the *in vitro* study was approximately 170 s, and it was approximately 130 s for the *in vivo* study. With the implementation of the applied approach on a GPU, the computational time could be significantly reduced. With addition of electrocardiography (ECG), accurately coupling the blood flow and the phase of the cardiac cycle would be possible. In this study, a lack of synchronized ECG was a limitation, which could be addressed with further development of the platform. Out-of-plane motion artifacts cannot be corrected with the current setup, which could be addressed by using a HFR 3-D scanning approach transmitting DWs [66]. Doppler-based strategies have been investigated for 3D motion correction in cardiac B-mode imaging using DWs [52], [67], [68]. It could be possible to translate our method to correct for motion in 3D, though to this end, many technical hurdles such as data handling, data transfer and data storage need to be overcome.

Coupling myocardium and vortex dynamics has been suggested for early diagnosis of LV filling impairment [60] but this requires a high temporal resolution. With the same pulse sequence, HFR B-mode imaging, contrast-mode imaging and 2-D vector blood flow mapping have been obtained simultaneously at 250 Hz as demonstrated in Section III-B. This provides a HFR triplex cardiac imaging tool using DWs, which could drastically improve our understanding of cardiac function by coupling myocardial motion, vortex dynamics in the LV and even microbubble-assisted myocardial perfusion.

V. CONCLUSION

This paper described the implementation of a motion correction method for HFR CEE using coherent DW imaging. Coherent summation of LRIs was corrupted without compensating for the motion between the angled DWs in both *in vitro* and *in vivo* studies. This method restored the image quality of a

rotating disk *in vitro* with an increase of 12 dB in CR and 7 dB in CNR within the investigated cyst areas. The application of motion correction retrieved microbubble signals in the LV *in vivo*, enabling the better contrasted myocardium. With the same pulse sequence, a HFR cardiac imaging technique using DWs was demonstrated by combining B mode, contrast mode, and 2-D vector blood flow mapping. Deciphering the interconnection between the simultaneous information (e.g., wall motion, vortex dynamics, and myocardial perfusion) obtained from these three imaging modes could be of clinical relevance for early diagnosis of cardiac dysfunction.

REFERENCES

[1] H. Mulvana *et al.*, "Characterization of contrast agent microbubbles for ultrasound imaging and therapy research," *IEEE Trans. Ultrason., Ferroelectr., Freq. Control*, vol. 64, no. 1, pp. 232–251, Jan. 2017.

[2] S. Qin, C. F. Caskey, and K. W. Ferrara, "Ultrasound contrast microbubbles in imaging and therapy: Physical principles and engineering," *Phys. Med. Biol.*, vol. 54, no. 6, p. R27, 2009.

[3] D. H. Simpson, C. T. Chin, and P. N. Burns, "Pulse inversion Doppler: A new method for detecting nonlinear echoes from microbubble contrast agents," *IEEE Trans. Ultrason., Ferroelectr., Freq. Control*, vol. 46, no. 2, pp. 372–382, Mar. 1999.

[4] R. J. Eckersley, C. T. Chin, and P. N. Burns, "Optimising phase and amplitude modulation schemes for imaging microbubble contrast agents at low acoustic power," *Ultrasound Med. Biol.*, vol. 31, no. 2, pp. 213–219, Feb. 2005.

[5] C. Tremblay-Darveau, R. Williams, L. Milot, M. Bruce, and P. N. Burns, "Combined perfusion and Doppler imaging using plane-wave nonlinear detection and microbubble contrast agents," *IEEE Trans. Ultrason., Ferroelectr., Freq. Control*, vol. 61, no. 12, pp. 1988–2000, Dec. 2014.

[6] C. Tremblay-Darveau, R. Williams, L. Milot, M. Bruce, and P. N. Burns, "Visualizing the tumor microvasculature with a nonlinear plane-wave Doppler imaging scheme based on amplitude modulation," *IEEE Trans. Med. Imag.*, vol. 35, no. 2, pp. 699–709, Feb. 2016.

[7] R. Olszewski *et al.*, "The clinical applications of contrast echocardiography," *Eur. J. Echocardiography*, vol. 8, no. 3, pp. s13–s23, 2007.

[8] R. Senior *et al.*, "Contrast echocardiography: Evidence-based recommendations by European association of echocardiography," *Eur. J. Echocardiogr.*, vol. 10, no. 2, pp. 194–212, 2009.

[9] T. R. Porter *et al.*, "Clinical applications of ultrasonic enhancing agents in echocardiography: 2018 American society of echocardiography guidelines update," *J. Amer. Soc. Echocardiogr.*, vol. 31, no. 3, pp. 241–274, 2018.

[10] M. Cikes, L. Tong, G. R. Sutherland, and J. D'Hooge, "Ultrafast cardiac ultrasound imaging: Technical principles, applications, and clinical benefits," *JACC Cardiovascular Imag.*, vol. 7, no. 8, pp. 812–823, Aug. 2014.

[11] J. Porée, D. Posada, A. Hodzic, F. Tournoux, G. Cloutier, and D. Garcia, "High-frame-rate echocardiography using coherent compounding with Doppler-based motion-compensation," *IEEE Trans. Med. Imag.*, vol. 35, no. 7, pp. 1647–1657, Jul. 2016.

[12] M. E. G. Toulemonde *et al.*, "High frame-rate contrast echocardiography: In-human demonstration," *JACC, Cardiovascular Imag.*, vol. 11, no. 6, pp. 923–924, 2018.

[13] S. Cimino *et al.*, "*In vivo* analysis of intraventricular fluid dynamics in healthy hearts," *Eur. J. Mechanics-B/Fluids*, vol. 35, pp. 40–46, Sep./Oct. 2012.

[14] D. P. Shattuck, M. D. Weinshenker, S. W. Smith, and O. T. von Ramm, "Explososcan: A parallel processing technique for high speed ultrasound imaging with linear phased arrays," *J. Acoust. Soc. Amer.*, vol. 75, no. 4, pp. 1273–1282, 1984.

[15] E. Boni, A. C. H. Yu, S. Freear, J. A. Jensen, and P. Tortoli, "Ultrasound open platforms for next-generation imaging technique development," *IEEE Trans. Ultrason., Ferroelectr., Freq. Control*, vol. 65, no. 7, pp. 1078–1092, Jul. 2018.

[16] L. Tong, A. Ramalli, R. Jasaityte, P. Tortoli, and J. D'hooge, "Multi-transmit beam forming for fast cardiac imaging–experimental validation and *in vivo* application," *IEEE Trans. Med. Imag.*, vol. 33, no. 6, pp. 1205–1219, Jun. 2014.

[17] L. Tong *et al.*, "Wide-angle tissue Doppler imaging at high frame rate using multi-line transmit beamforming: An experimental validation *in vivo*," *IEEE Trans. Med. Imag.*, vol. 35, no. 2, pp. 521–528, Feb. 2016.

[18] G. Zurakhov *et al.*, "Multiline transmit beamforming combined with adaptive apodization," *IEEE Trans. Ultrason., Ferroelectr., Freq. Control*, vol. 65, no. 4, pp. 535–545, Apr. 2018.

[19] P. Santos, L. Tong, A. Ortega, L. Løvstakken, E. Samset, and J. D'hooge, "Acoustic output of multi-line transmit beamforming for fast cardiac imaging: A simulation study," *IEEE Trans. Ultrason., Ferroelectr., Freq. Control*, vol. 62, no. 7, pp. 1320–1330, Jul. 2015.

[20] H. Hasegawa and H. Kanai, "High-frame-rate echocardiography using diverging transmit beams and parallel receive beamforming," *J. Med. Ultrason.*, vol. 38, no. 3, pp. 129–140, 2011.

[21] C. Papadacci, M. Pernot, M. Couade, M. Fink, and M. Tanter, "High-contrast ultrafast imaging of the heart," *IEEE Trans. Ultrason., Ferroelectr., Freq. Control*, vol. 61, no. 2, pp. 288–301, Feb. 2014.

[22] B.-F. Osmanski, D. Maresca, E. Messas, M. Tanter, and M. Pernot, "Transthoracic ultrafast Doppler imaging of human left ventricular hemodynamic function," *IEEE Trans. Ultrason., Ferroelectr., Freq. Control*, vol. 61, no. 8, pp. 1268–1275, Aug. 2014.

[23] J. Grondin, V. Sayseng, and E. E. Konofagou, "Cardiac strain imaging with coherent compounding of diverging waves," *IEEE Trans. Ultrason., Ferroelectr., Freq. Control*, vol. 64, no. 8, pp. 1212–1222, Aug. 2017.

[24] S. Fadnes, M. S. Wigen, S. A. Nyrnes, and L. Lovstakken, "*In vivo* intracardiac vector flow imaging using phased array transducers for pediatric cardiology," *IEEE Trans. Ultrason., Ferroelectr., Freq. Control*, vol. 64, no. 9, pp. 1318–1326, Sep. 2017.

[25] M. Toulemonde *et al.*, "Cardiac imaging with high frame rate contrast enhanced ultrasound: In-vivo demonstration," in *Proc. IEEE Int. Ultrason. Symp. (IUS)*, Sep. 2016, pp. 1–4.

[26] K. S. Kim, J. S. Hwang, J. S. Jeong, and T. K. Song, "An efficient motion estimation and compensation method for ultrasound synthetic aperture imaging," *Ultrason. Imag.*, vol. 24, no. 2, pp. 81–99, Apr. 2002.

[27] B. Y. S. Yiu, I. K. H. Tsang, and A. C. H. Yu, "A modified synthetic aperture imaging approach with axial motion compensation," in *Proc. IEEE Ultrason. Symp. (IUS)*, Nov. 2008, pp. 1254–1257.

[28] K. L. Gammelmark and J. A. Jensen, "2-D tissue motion compensation of synthetic transmit aperture images," *IEEE Trans. Ultrason., Ferroelectr., Freq. Control*, vol. 61, no. 4, pp. 594–610, Apr. 2014.

[29] Y.-H. Chen, Y.-M. Lin, K.-Y. Ho, A.-Y. Wu, and P.-C. Li, "Low-complexity motion-compensated beamforming algorithm and architecture for synthetic transmit aperture in ultrasound imaging," *IEEE Trans. Signal Process.*, vol. 62, no. 4, pp. 840–851, Feb. 2014.

[30] B. Denarie *et al.*, "Coherent plane wave compounding for very high frame rate ultrasonography of rapidly moving targets," *IEEE Trans. Med. Imag.*, vol. 32, no. 7, pp. 1265–1276, Jul. 2013.

[31] I. K. Ekroll, M. M. Voormolen, O. K.-V. Standal, J. M. Rau, and L. Lovstakken, "Coherent compounding in Doppler imaging," *IEEE Trans. Ultrason., Ferroelectr., Freq. Control*, vol. 62, no. 9, pp. 1634–1643, Sep. 2015.

[32] J. Voorneveld *et al.*, "High frame rate ultrasound particle image velocimetry for estimating high velocity flow patterns in the left ventricle," *IEEE Trans. Ultrason., Ferroelectr., Freq. Control*, vol. 65, no. 21, pp. 2222–2232, Dec. 2017.

[33] P. Joos *et al.*, "High-frame-rate speckle-tracking echocardiography," *IEEE Trans. Ultrason., Ferroelectr., Freq. Control*, vol. 65, no. 5, pp. 720–728, May 2018.

[34] S. Harput *et al.*, "Two-stage motion correction for super-resolution ultrasound imaging in human lower limb," *IEEE Trans. Ultrason., Ferroelectr., Freq. Control*, vol. 65, no. 5, pp. 803–814, May 2018.

[35] M. Toulemonde *et al.*, "Effects of motion on high frame rate contrast enhanced echocardiography and its correction," in *Proc. IEEE Int. Ultrason. Symp.*, Washington, DC, USA, Sep. 2017, pp. 1–4.

[36] C. H. Leow, E. Bazigou, R. J. Eckersley, C. Alfred, P. D. Weinberg, and M.-X. Tang, "Flow velocity mapping using contrast enhanced high-frame-rate plane wave ultrasound and image tracking: Methods and initial *in vitro* and *in vivo* evaluation," *Ultrasound Med., Biol.*, vol. 41, no. 11, pp. 2913–2925, 2015.

[37] L. Nie, S. Harput, D. M. J. Cowell, and S. Freear, "Velocity estimation error reduction in stenosis areas using a correlation correction method," in *Proc. IEEE Int. Ultrason. Symp. (IUS)*, Sep. 2016, pp. 1–4.

[38] L. Niu *et al.*, "Ultrasonic particle image velocimetry for improved flow gradient imaging: Algorithms, methodology and validation," *Phys. Med. Biol.*, vol. 55, no. 7, p. 2103, 2010.

[39] F. Scarano, "Iterative image deformation methods in PIV," *Meas. Sci. Technol.*, vol. 13, no. 1, p. R1, 2001.

[40] J. Westerweel and F. Scarano, "Universal outlier detection for PIV data," *Experim. Fluids*, vol. 39, no. 6, pp. 1096–1100, 2005.

[41] D. Garcia, "Robust smoothing of gridded data in one and higher dimensions with missing values," *Comput. Statist. Data Anal.*, vol. 54, no. 4, pp. 1167–1178, Apr. 2010.

[42] D. Cowell and S. Freear, "Quinary excitation method for pulse compression ultrasound measurements," *Ultrasonics*, vol. 48, no. 2, pp. 98–108, 2008.

[43] P. R. Smith, D. M. J. Cowell, and S. Freear, "Width-modulated square-wave pulses for ultrasound applications," *IEEE Trans. Ultrason., Ferroelectr., Freq. Control*, vol. 60, no. 11, pp. 2244–2256, Nov. 2013.

[44] R. E. Apfel and C. K. Holland, "Gauging the likelihood of cavitation from short-pulse, low-duty cycle diagnostic ultrasound," *Ultrasound Med. Biol.*, vol. 17, no. 2, pp. 179–185, Jan. 1991.

[45] C. C. Church, "Frequency, pulse length, and the mechanical index," *Acoust. Res. Lett. Online*, vol. 6, no. 3, pp. 162–168, 2005.

[46] Z. Alomari, S. Harput, S. Hyder, and S. Freear, "Selecting the number and values of the CPWI steering angles and the effect of that on imaging quality," in *Proc. IEEE Int. Ultrason. Symp.*, Sep. 2014, pp. 1191–1194.

[47] J. A. Jensen and N. B. Svendsen, "Calculation of pressure fields from arbitrarily shaped, apodized, and excited ultrasound transducers," *IEEE Trans. Ultrason., Ferroelectr., Freq. Control*, vol. 39, no. 2, pp. 262–267, Mar. 1992.

[48] E. Be'eri, S. E. Maier, M. J. Landzberg, T. Chung, and T. Geva, "*In vivo* evaluation of Fontan pathway flow dynamics by multidimensional phase-velocity magnetic resonance imaging," *Circulation*, vol. 98, no. 25, pp. 2873–2882, 1998.

[49] S. K. Jespersen, J. E. Wilhjelm, and H. Sillesen, "Multi-angle compound imaging," *Ultrason. Imag.*, vol. 20, pp. 81–102, Apr. 1998.

[50] L. Nie, S. Harput, D. M. J. Cowell, T. M. Carpenter, J. R. Mclaughlan, and S. Freear, "Combining acoustic trapping with plane wave imaging for localized microbubble accumulation in large vessels," *IEEE Trans. Ultrason., Ferroelectr., Freq. Control*, vol. 65, no. 7, pp. 1193–1204, Jul. 2018.

[51] J. E. Browne, K. V. Ramnarine, A. J. Watson, and P. R. Hoskins, "Assessment of the acoustic properties of common tissue-mimicking test phantoms," *Ultrasound Med. Biol.*, vol. 29, no. 7, pp. 1053–1060, Jul. 2003.

[52] Y. Chen, J. D'hooge, and J. Luo, "Doppler-based motion compensation strategies for 3-D diverging wave compounding and multiplane-transmit beamforming: A simulation study," *IEEE Trans. Ultrason., Ferroelectr., Freq. Control*, vol. 65, no. 9, pp. 1631–1642, Sep. 2018.

[53] M. Toulemonde *et al.*, "High-frame-rate contrast echocardiography using diverging waves: Initial *in-vitro* and *in-vivo* evaluation," *IEEE Trans. Ultrason., Ferroelectr., Freq. Control*, vol. 65, no. 12, pp. 2212–2221, Dec. 2018.

[54] A. E. Saris, H. H. Hansen, S. Fekkes, M. M. Nillesen, M. C. Rutten, and C. L. de Korte, "A comparison between compounding techniques using large beam-steered plane wave imaging for blood vector velocity imaging in a carotid artery model," *IEEE Trans. Ultrason., Ferroelectr., Freq. Control*, vol. 63, no. 11, pp. 1758–1771, Nov. 2016.

[55] H. B. Kim, J. R. Hertzberg, and R. Shandas, "Development and validation of echo PIV," *Exp. Fluids*, vol. 36, no. 3, pp. 455–462, Mar. 2004.

[56] M. Lenge, A. Ramalli, E. Boni, H. Liebgott, C. Cachard, and P. Tortoli, "High-frame-rate 2-D vector blood flow imaging in the frequency domain," *IEEE Trans. Ultrason., Ferroelectr., Freq. Control*, vol. 61, no. 9, pp. 1504–1514, Sep. 2014.

[57] J. Westerweel, "Fundamentals of digital particle image velocimetry," *Meas. Sci. Technol.*, vol. 8, no. 12, p. 1379, 1997.

[58] F. Lin, C. Cachard, R. Mori, F. Varray, F. Guidi, and O. Basset, "Ultrasound contrast imaging: Influence of scatterer motion in multi-pulse techniques," *IEEE Trans. Ultrason., Ferroelectr., Freq. Control*, vol. 60, no. 10, pp. 2065–2078, Oct. 2013.

[59] M.-X. Tang *et al.*, "Quantitative contrast-enhanced ultrasound imaging: A review of sources of variability," *Interface Focus*, vol. 1, no. 4, pp. 520–539, May 2011.

[60] J. Faurie, M. Baudet, J. Porée, G. Cloutier, F. Tournoux, and D. Garcia, "Coupling myocardium and vortex dynamics in diverging-wave echocardiography," *IEEE Trans. Ultrason., Ferroelectr., Freq. Control*, to be published, doi: 10.1109/TUFFC.2018.2842427.

[61] C. Kasai, K. Namekawa, A. Koyano, and R. Omoto, "Real-time two-dimensional blood flow imaging using an autocorrelation technique," *IEEE Trans. Sonics Ultrason.*, vol. SU-32, no. 3, pp. 458–464, May 1985.

[62] T. Loupas, J. T. Powers, and R. W. Gill, "An axial velocity estimator for ultrasound blood flow imaging, based on a full evaluation of the Doppler equation by means of a two-dimensional autocorrelation approach," *IEEE Trans. Ultrason., Ferroelectr., Freq. Control*, vol. 42, no. 4, pp. 672–688, Jul. 1995.

[63] M. Ressner, T. Jansson, J. Cedefamn, P. Ask, and B. Janerot-Sjoberg, "Contrast biases the autocorrelation phase shift estimation in Doppler tissue imaging," *Ultrasound Med., Biol.*, vol. 35, no. 3, pp. 447–457, 2009.

[64] D. Rueckert, L. I. Sonoda, C. Hayes, D. L. G. Hill, M. O. Leach, and D. J. Hawkes, "Nonrigid registration using free-form deformations: Application to breast MR images," *IEEE Trans. Med. Imag.*, vol. 18, no. 8, pp. 712–721, Aug. 1999.

[65] D.-J. Kroon. *B-Spline Grid, Image and Point Based Registration*. Accessed: Aug. 14, 2018. [Online]. Available: https://uk.mathworks.com/matlabcentral/fileexchange/20057-b-spline-grid-image-and-point-based-registration/

[66] E. Roux, F. Varray, L. Petrusca, C. Cachard, P. Tortoli, and H. Liebgott, "Experimental 3-D ultrasound imaging with 2-D sparse arrays using focused and diverging waves," *Sci. Rep.*, vol. 8, no. 1, p. 9108, 2018.

[67] P. Joos *et al.*, "High-frame-rate 3-D echocardiography based on motion compensation: An *in vitro* evaluation," in *Proc. IEEE Int. Ultrason. Symp. (IUS)*, Sep. 2017, pp. 1–4.

[68] P. Joos *et al.*, "High-volume-rate 3-d ultrasound imaging based on motion compensation: A feasibility study," in *Proc. IEEE Int. Ultrason. Symp. (IUS)*, Sep. 2017, p. 1.

Luzhen Nie (S'16) received the M.Eng. degree in electronic and electrical engineering from the Harbin Institute of Technology, Harbin, China, in 2015. He is currently pursuing the Ph.D. degree with the Ultrasonics and Instrumentation Group, University of Leeds, Leeds, U.K.

His current research interests involve high-frame-rate ultrasound imaging, microbubble contrast agents, and blood flow and Doppler imaging.

David M. J. Cowell received the Ph.D. degree from the University of Leeds, Leeds, U.K., in 2008, for research on advanced coding techniques and excitation circuit design for industrial instrumentation and medical imaging ultrasound systems.

He performed extensive consultancy in instrumentation, field-programmable gate arrays, and high-speed digital hardware design. Following work as a Research Consultant in measurement and instrumentation, he joined the Ultrasound Group, University of Leeds, as a Research Fellow, where his research is currently focused on noninvasive industrial ultrasound measurement and advanced miniaturized ultrasound excitation systems with low harmonic distortion for phased array imaging, ultrasound system design, and signal processing.

Thomas M. Carpenter received the M.Eng. degree in electronic and electrical engineering from the University of Leeds, Leeds, U.K., in 2014, where he is currently pursuing the Ph.D. degree with the Ultrasound Group.

He joined the Georgia Institute of Technology, Atlanta, GA, USA, as a Research Engineer, developing high-speed FPGA designs for ultrasound imaging applications. He is currently a Research Assistant with the Ultrasound Group, University of Leeds. His main research focus is embedded systems and FPGA design, both in the biomedical field and for industrial applications.

James R. McLaughlan received the Ph.D. degree from the Institute of Cancer Research, London, U.K., with a focus on the optimization of therapeutic ultrasound for cancer therapy using cavitation.

In 2010, he joined the University of Leeds, Leeds, U.K., to work on next-generation therapeutic microbubbles. He currently holds a joint academic position between the Faculties of Engineering and Medicine and Health, where his main research areas are noninvasive cancer therapies, molecular-targeted theranostics, and semi-autonomous surgical systems.

Dr. McLaughlan was a recipient of the Leverhulme Early Career Research Fellowship, in 2013, to develop molecular-targeted gold nanoparticles for the detection and treatment of cancerous cells within breast tissue.

Arzu A. Çubukçu received the degree from Istanbul Medical Faculty, Istanbul, Turkey, in 1985. She received the Ph.D. from the University of Leeds, Leeds, U.K., in 2000, where she focused on stress MRI and echocardiogram in the prediction of myocardial functional recovery following revascularisation procedures.

She completed medical specialist training in Istanbul, followed by research in cardiology, and focused on cardiac ultrasound and subsequently MRI at the University of Leeds. Since 2000, she has been a Consultant Cardiologist with East Cheshire NHS Trust. She specializes in clinical cardiology and cardiac imaging, predominantly with ultrasound, and more recently with Cardiac CT.

Steven Freear (S'95–M'97–SM'11) received the Ph.D. degree from the University of Leeds, Leeds, U.K., in 1997.

He worked in the electronics industry for seven years as a medical ultrasonic system designer. He was appointed as a Lecturer (Assistant Professor), a Senior Lecturer (Associate Professor), and then a Professor with the School of Electronic and Electrical Engineering, University of Leeds, in 2006, 2008, and 2016, respectively. In 2006, he formed the Ultrasound Group, specializing in both industrial and biomedical research. In 2014, he was appointed as a Visiting Professor with the Georgia Institute of Technology, Atlanta, GA, USA. He is currently an External Examiner to undergraduate programs in electronic engineering with Queen's University Belfast, Belfast, U.K. He teaches digital signal processing, VLSI and embedded systems design, and hardware description languages at both undergraduate and postgraduate levels. His main research interest is concerned with advanced analog and digital signal processing and instrumentation for ultrasonic systems.

Dr. Freear was the recipient of the 2018 IEEE UFFC-S Distinguished Service Award. He was elected as the Editor-in-Chief of the IEEE TRANSACTIONS ON ULTRASONICS, FERRORELECTRICS AND FREQUENCY CONTROL in 2013.